Catalysis Today 144 (2009) 19–25

Contents lists available at ScienceDirect

Catalysis Today

journal homepage: www.elsevier.com/locate/cattod

Visible light-activated N-F-codoped TiO_2 nanoparticles for the photocatalytic degradation of microcystin-LR in water☆

Miguel Pelaez [a], Armah A. de la Cruz [b], Elias Stathatos [c], Polycarpos Falaras [d], Dionysios D. Dionysiou [a,*]

[a] Department of Civil and Environmental Engineering, University of Cincinnati, Cincinnati, OH 45221-0071, USA
[b] Office of Research and Development, U.S. Environmental Protection Agency, Cincinnati, OH 45268, USA
[c] Electrical Engineering Department, Technological-Educational Institute of Patras 26334 Patras, Greece
[d] Institute of Physical Chemistry, NCSR Demokritos, 15310 Aghia Paraskevi, Attiki, Greece

ARTICLE INFO

Article history:
Available online 31 January 2009

Keywords:
Visible light
Microcystin-LR
Titanium dioxide
Photocatalysis
Fluorine doping
Nitrogen doping
Sol–gel method

ABSTRACT

In this study, we developed nonmetal-doped TiO_2 nanoparticles (N-F-TiO_2) by a novel synthesis route employing a simple sol–gel method containing a nonionic fluorosurfactant as pore template material to tailor-design the structural properties of TiO_2 and fluorine dopant as well as ethylenediamine as nitrogen source for the photocatalytic response towards visible light. The synthesized photocatalyst was characterized by XRD, UV–vis spectroscopy, XPS, HR-TEM, ESEM and porosimetry measurements. The resulting nanoparticles exhibited enhanced structural properties such as high surface area (141 m^2/g), high porosity (49%), mesoporous structure (2–10 nm pore size) and low degree of agglomeration (1.07). A reduction in the effective band gap (2.75 eV) was observed compared with reference TiO_2 (3.00 eV) due to the red-shift in the optical absorption spectrum of the nonmetal-doped TiO_2 photocatalyst. We also focused on the environmental application of the prepared nanoparticles for the destruction of microcystin-LR (MC-LR) under visible light irradiation ($\lambda > 420$ nm). Under acidic conditions (pH 3.0 ± 0.1), the highest MC-LR degradation rate was achieved with N-F-TiO_2. The electrostatic interactions between the toxin and the N-F-codoped TiO_2 favored the photocatalytic degradation. Beneficial effects induced by codoping with nitrogen and fluorine are responsible for higher photocatalytic activity than TiO_2 nanoparticles with only fluorine or nitrogen doping. Also, commercially available visible light-activated TiO_2 showed lower degradation rate per unit surface area of the material.

1. Introduction

The development of nanotechnology for the synthesis of nanomaterials is providing unprecedented opportunities to deal with emerging environmental problems associated with water contamination along with worldwide energy-related concerns [1]. Currently, advanced oxidation technologies (AOTs) and nanotechnologies (AONs) have been extensively investigated for the destruction of toxic and recalcitrant organic compounds and inactivation of microorganisms in water and air [2–12]. Titanium dioxide (TiO_2), a well-known semiconductor with photocatalytic properties, is a widely used AON for water and air remediation [6–10]. It has proven to be highly effective in the nonselective degradation of organic contaminants due to high decomposition and mineralization rates. However, conventional TiO_2 requires ultraviolet (UV) radiation ($\lambda < 400$ nm) to overcome its wide band gap energy (~3.2 eV for anatase phase) for photocatalytic activation [4,11]. This is a technological limitation when aiming at implementation of large scale sustainable technologies with renewable energy sources such as solar light, since UV radiation accounts only for 5% of the total solar spectrum compared to the visible region (~45%) [12,13]. Several attempts have been directed towards the development of modified TiO_2 with visible light response by dye sensitization, metal (Fe, Co, Ag) [14,15] and nonmental (N, F, C, S) [4,16–23] doping of the catalyst to reduce TiO_2 band gab energy requirements for photocatalytic activation. In some metal doping approaches, the resulting visible light photocatalytic activity has some drawbacks including increase in the carrier-recombination centers (electron–hole pair species generated after photo-excitation of the catalyst) and low thermal stability of the modified material [14]. Moreover, metal leaching and possible toxicity diminish the potential of employing metal-doped TiO_2 for drinking and wastewater treatment applications. A more successful approach involves nonmetal doping of TiO_2. Nitrogen doping of TiO_2 for visible-light driven photocatalysis revealed band gap narrowing from the mixing of nitrogen 2p states with oxygen 2p states on the top of the valence band at

☆ *Disclaimer*: Although this work was reviewed by the US EPA and approved for publication, it may not necessarily reflect official Agency policy. Mention of trade names and commercial products do not constitute endorsement or recommendation for use.

* Corresponding author. Tel.: +1 513 556 0724; fax: +1 513 556 2599.
E-mail address: dionysios.d.dionysiou@uc.edu (D.D. Dionysiou).

0920-5861/$ – see front matter © 2009 Elsevier B.V. All rights reserved.
doi:10.1016/j.cattod.2008.12.022

substitutional lattice sites in the form of nitride (Ti–N) or oxynitride (Ti–O–N). A different arrangement is the formation of oxyanion species at the interstitial lattice sites creating localized intergap states [24]. Both configurations make it possible to shift the optical absorption towards visible light, thus, allowing photocatalytic activity in the visible region [11,22,23]. Fluorine doping is also effective to induce modifications of the electronic structure of TiO_2 by the creation of surface oxygen vacancies due to charge compensation between F^- and Ti^{4+} but without producing a significant change in the optical absorption of TiO_2 [21]. Moreover, codoping of TiO_2 with nitrogen and fluorine has demonstrated high photocatalytic activity in the visible region with beneficial effects induced by both dopants [25–27]. Huang et al. confirmed strong visible-light absorption and high photocatalytic activity of N-F-TiO_2 for *p*-chlorophenol and Rhodamine B degradation under visible light irradiation [26]. Xie et al. effectively decomposed methyl orange with visible light-induced N-F-TiO_2 photocatalyst [27]. Both attributed their findings to the synergistic effect of nitrogen and fluorine doping.

In addition to nonmetal doping, structural properties of TiO_2 are of significant importance to enhance its physicochemical properties and photocatalytic response. For instance, the use of self-assembly surfactant-based sol–gel methods has been reported as an effective approach to tailor-design the structural properties of TiO_2 nanoparticles and films from molecular precursors [6,8–10]. The hydrocarbon surfactant is used as pore directing agent and to control the hydrolysis and condensation rates of the titanium precursor in the sol formulation. This method has the capacity to yield tailor-designed TiO_2 with high surface area, high porosity, small crystal size with narrow pore size distribution and high photocatalytic activity under UV [8–10] and visible light irradiation [4].

One of the aims of this work is to develop highly efficient N-F-codoped TiO_2 nanoparticles with enhanced structural properties and high photocatalytic activity under visible light irradiation using a novel sol–gel route employing a nonionic fluorosurfactant as pore directing agent and fluorine dopant and ethylenediamine as nitrogen source. Fluorosurfactants or fluorinated surfactants, have been used mainly as antistatic, antifogging and wetting agents, and paint coating additives [28]. Only recent studies have focused on the use of fluorinated surfactants as pore template for mesoporous silica materials [29–32], signifying a great potential for novel ceramic materials.

The second aim of this work is to focus on the application of such nanoparticles in engineered water treatment processes for the destruction of environmental contaminants of worldwide concern. Drinking water treatment plants are facing more prevalent occurrence of cyanobacterial harmful algae blooms (Cyano-HABs) and the release of their toxins in their water sources. These toxins are considered a serious health risk due to their high solubility in water, toxicity (i.e., hepatotoxicity, neurotoxicity, and carcinogenicity) and chemical stability. Among them, microcystin-LR (MC-LR) is one of the most commonly found cyanotoxins in Cyano-HABs and the most toxic derivative of the group of microcystins [33]. Conventional TiO_2 has been proven to be effective in the treatment of MC-LR under UV radiation [34,35]. Recent work demonstrated high degradation rates of MC-LR with nitrogen-doped TiO_2 nanoparticles [4]. In this study, we present results on the destruction of MC-LR with N-F-TiO_2 nanoparticles under visible light irradiation.

2. Experimental

2.1. Synthesis of visible light-activated TiO_2 nanoparticles

To prepare the modified sol–gel solution, a nonionic fluorosurfactant (Zonyl FS-300 (FS), ~50% solids in H_2O, $R_fCH_2CH_2O(CH_2CH_2O)_xH$; $R_f = F(CF_2CF_2)_y$ where $x = 14$ and $y = 3$, Fluka), acting as both pore directing agent and fluorine source, dissolved in isopropanol (i-PrOH), was used. Acetic acid (Fisher) was added to maintain a low pH (~6.4). Before adding the titania precursor, anhydrous ethylenediamine (EDA, Fisher) was added in the solution as nitrogen source. Then, titanium(IV) isopropoxide (TTIP, 97%, Aldrich) was added dropwise under vigorous stirring and more acetic acid was added for peptidization. The final sol obtained was transparent, homogeneous and stable after stirred overnight at room temperature. Afterwards, the sol was dried at room temperature for 24 h and then calcined in a multi-segment programmable furnace (Paragon HT-22-D, Thermcraft) where the temperature was increased at a ramp rate of 60 °C/h to 100 °C and maintained for 1 h. Then it was increased up to 400 °C under the same ramp rate, maintained for 2 h and cooled down naturally to finally obtain a yellowish powder. The FS:i-PrOH:acetic acid:EDA:TTIP molar ratio employed in the sol–gel for the preparation of the denoted Particle 1 was 0.01:0.65:1.0:0.1:0.05. Specifically, the i-PrOH/EDA molar ratio was 2.85 and 14 for Particles 2, and 3, respectively. Nitrogen-doped TiO_2 (Particle 4) and fluorine-doped TiO_2 (Particle 5) where synthesized without FS and EDA, respectively, maintaining the same final volume by the addition of more isopropanol. Reference TiO_2 was synthesized using the same procedure but without the addition of nitrogen and fluorine sources. The synthesized nanoparticles were compared with Kronos vlp 7000, a commercially available visible light-activated TiO_2 photocatalyst (Kronos International Inc., D-51373).

2.2. Characterization of synthesized TiO_2

An X-ray diffraction (XRD) analysis was performed with a Kristalloflex D500 diffractometer (Siemens) using Cu Kα (λ = 1.5406 Å) radiation, to study the crystal structure and crystallinity of the TiO_2 nanoparticles. The Brunauer–Emmett–Teller (BET) surface area, pore volume, porosity, Barret–Joyner–Halenda (BJH) pore size and distribution (based on nitrogen adsorption and desorption isotherms) were determined by Tristar 300 (Micromeritics) porosimeter analyzer. The samples were purged with nitrogen gas for 2 h at 150 °C using Flow prep 060 (Micromeritics). A high resolution-transmission electron microscope (HR-TEM) with field emission gun at 200 kV was employed to obtain crystal size and crystal structure at the nanoscale. The samples in ethanol were dispersed using an ultrasonicator (2510R-DH, Bransonic) for 15 min and fixed on a carbon-coated copper grid (LC200-Cu, EMS). The particle morphology was characterized by an environmental scanning electron microscope (ESEM, Philips XL 30 ESEM-FEG) at an accelerating voltage of 30 kV. The point of zero charge (PZC) was measured using a Zetasizer (Malvern Instruments). The fine elemental composition and electronic structure was determined with an X-ray photoelectron spectroscope (XPS, PerkinElmer Model 5300) with Mg Kα X-rays at a takeoff angle of 45° and vacuum pressure of 10^{-8} to 10^{-9} Torr. The binding energies were calibrated with respect to C_{1s} core level peak at 284.6 eV. To investigate the optical band gap of the synthesized TiO_2 nanoparticles, the UV–vis absorption spectra were obtained with a UV–vis spectrophotometer (Shimadzu 2501 PC) mounted with an integrating sphere accessory (ISR1200) using $BaSO_4$ as reference standard.

2.3. Photocatalytic evaluation with microcystin-LR under visible light

The photocatalytic activity of the synthesized TiO_2 nanoparticles was evaluated for the degradation of MC-LR. A borosilicate vessel (i.d. 4.7 cm) was employed as photocatalytic reactor. An aqueous solution, previously adjusted at the desired pH with H_2SO_4 or NaOH without any buffer, was spiked with an aliquot of

MC-LR standard (Calbiochem Cat #. 475815) to achieve an initial concentration of 1.0 ± 0.05 mg/L. A solution with TiO_2 nanoparticles was dispersed using an ultrasonicator (2510R-DH, Bransonic) for 24 h and transferred to the reactor containing MC-LR for a final volume solution of 10 ml. The reactor was completely sealed and mixed to minimize mass transfer limitations. Two 15 W fluorescent lamps (Cole-Parmer) mounted with UV block filter (UV420, Opticology) to eliminate spectral range below 420 nm were employed to irradiate the reactors. The intensity of the radiation was below the detection limit when employing an IL 1700 radiometer (International Light) with a 365 nm sensor. The light intensity was determined using a broadband radiant power meter (Newport Corporation) for a total visible light intensity of 7.81×10^{-5} W cm^{-2}. During irradiation, a fan was positioned near the reactor to cool it down. Sampling was done at specific periods of time and the samples were quenched with methanol to stop any further reaction, filtered (L815, Whatman) to remove the suspended nanoparticles, transferred to 0.2 ml glass inserts and placed in sample vials. MC-LR samples were analyzed by liquid chromatography (LC, Agilent Series 1100) equipped with a photodiode array detector set at 238 nm under isocratic conditions: 60% (v/v) of 0.05% trifluoroacetic acid (TFA) in MilliQ water and 40% (v/v) of 0.05% TFA in acetonitrile with a flow rate of 1 ml/min. The column employed was a C_{18} Discovery (Supelco) column (4.6 mm × 150 mm, 3 μm particle size) kept at 40 °C with an injection volume of 50 μl [7]. The handling of the toxin must be done with extreme care since it is highly toxic and irritant if exposed. Therefore, all the experiments were conducted in an Advance Sterilchemgard III Class II biological safety cabinet (Baker Company, Sanford, ME) with full exhaust.

3. Results and discussion

3.1. Nanoparticle synthesis method

It is well known that above the critical micelle concentration (CMC), surfactants form well-defined self-assembled micelle structures in solution. Fluorosurfactants have a lower CMC in water than hydrocarbon surfactants so they can also assemble more easily in solution and form small-pore mesoporous materials [29–32]. Tan et al. obtained highly porous silica nanoparticles with a short-chain fluorosurfactant at low concentration resulting in small, uniform pores [29]. In such method, after the fluorosurfactant self-assemble in a micelle formation in the modified sol–gel, the nitrogen atoms (N) of ethylenediamine act as a ligand with the Ti atoms, after the addition of TTIP, forming an insoluble coordination compound or adduct by the bonding of N with Ti [36]. This coordination compound is positioned around the micelle creating an inorganic–organic composite material. The hydrolysis and condensation of Ti precursor are influenced by the adduct formation and the presence of the fluorosurfactant (see Section 3.2). During heat treatment of the composite material, the fluorosurfactant is removed leaving a porous structure and fluorine atoms are diffuse into the lattice of TiO_2 substituting some oxygen atoms with fluorine atoms. Nitrogen atoms are already incorporated in the adduct coordination compound even before calcination [4]. As the material is heat treated, TiO_2 crystallization increases and nitrogen can diffuse and distribute throughout the TiO_2 lattice (see Section 3.4 for XPS depth profile).

3.2. Structural characteristics of TiO_2 nanoparticles

All peaks on the XRD patterns of the different nonmetal-doped and reference TiO_2 samples (see Fig. 1S) were designated to anatase crystal phase (most active phase) without any indication of other crystalline phases, such as rutile or dopant related, under the analyzed conditions. The crystalline size of the nonmetal-doped nanoparticles range from 8.7 to 10.2 nm and that of the reference sample was 12.1 nm (see Table 1) indicating a clear broader peak in the 101 plane for the synthesized TiO_2. No significant variation of the d_{space} in the 1 0 1 plane, $D_{(1\,0\,1)}$, was found between all the nanoparticles and the reference sample. The incorporation of nitrogen or fluorine did not result in a significant change in the average unit cell dimension since the bond lengths of Ti–N (1.940 and 2.042 Å) and Ti–F (2.022 and 2.253 Å) are similar to those of Ti–O bonds (1.940 and 2.000 Å). Even though nitrogen atom has a higher radius (0.65 Å) compared to oxygen atom (0.60 Å) and fluorine (0.57 Å), the modifications are minor and the resultant doping suggests a paramagnetic impurity [17,25]. The low doping percentage may also be responsible for the insignificant changes in the crystalline structure.

Other physicochemical properties are listed in Table 1. The structural properties were significantly improved with the addition of fluorosurfactant and ethylenediamine compared to reference TiO_2. During heat treatment, the fluorosurfactant and other organic residues were removed creating a pore structure. The BET surface area was significantly high, 141 m^2/g for Particle 1, and increasing the i-PrOH/EDA molar ratio resulted in a slight decrease of the surface area and pore volume. The fluorosurfactant effectively worked as pore directing agent during the synthesis of the nanoparticles and ethylenediamine can contribute in the hydrolysis and condensation rate of TiO_2 [36]. In solution, fluorosurfactants have similar phase behavior to hydrocarbon surfactants and can be employed for the preparation of mesoporous materials. For nonionic surfactants, one CF_2 group is equivalent to 1.7 CH_2 groups which leads to lower CMCs [32]. The CMC of the fluorosurfactant employed in aqueous solution is 0.61 mmol/L [28], much lower than the concentration added in the sol–gel formulation (78.6 mmol/L) employed in this study. In the absence of fluorosurfactant, the surface area was reduced significantly and the crystal size was relatively larger for Particle 5. However, since the nitrogen atoms of ethylenediamine act as a ligand with the titanium alkoxide to form a coordination compound, this adduct formation may influence the hydrolysis and condensation rates of the metal alkoxide in the sol–gel. It can restrict TiO_2 growth leading to pore surface modification and the size of the anatase crystal may be reduced [36,37]. With a decrease in crystal size, the

Table 1
Physicochemical properties of reference TiO_2 and Particles 1–5 by the modified sol–gel method.

Sample	Crystal phase	Crystal size[a] (nm)	$D_{(1\,0\,1)}$ (Å)	BET surface area (m^2/g)	Crystal size[b] (nm)	Pore volume (cm^3/g)	Porosity (%)	PZC	Degree of agglomeration (DA)
Reference	Anatase	12.1	3.520	33.6	45.9	0.087	25.3	5.6	3.79
Particle 1	Anatase	8.7	3.516	141.6	10.9	0.248	49.1	5.9	1.27
Particle 2	Anatase	8.6	3.514	153.0	10.1	0.308	54.5	6.0	1.18
Particle 3	Anatase	10.0	3.514	119.3	12.9	0.249	49.2	5.9	1.29
Particle 4	Anatase	10.2	3.517	115.9	13.3	0.192	42.8	6.0	1.30
Particle 5	Anatase	9.3	3.517	83.3	18.5	0.114	30.7	5.9	2.00

[a] Obtained from XRD, using Scherrer equation: $D = 0.9\lambda/(B \times \cos\theta)$, where $\lambda = 0.154$ nm and B = Full Width at Half Maximum (FWHM) of the highest peak.
[b] Obtained from BET, using $D = 6000/(\rho \times$ BET surface area), where $\rho = 3.89$ g/cm^3 of anatase density.

BET surface area becomes higher. Burda et al. obtained nitrogen-doped TiO_2 nanoparticles, employing ethylenediamine, with a surface area between 80 and 120 m^2/g using a surfactant-free sol–gel procedure [2].

The mechanism of a porous structure is related to the role of the surfactant [8–10]. The geometry of the micelles that are formed by the fluorosurfactant employed in a water-rich environment consists of close-packed spherical micelles. With these types of micelles the typical resulting pores are spherical and they are in agreement with HR-TEM images (see Fig. 3S). The presence of a significant hysteresis loop in the adsorption–desorption isotherms indicates that the synthesized nonmetal-doped TiO_2 particles were type IV, typical for mesoporous materials. This proves the pore size controllability of those nanoparticles where the fluorosurfactant was added during their synthesis (note Fig. 2Sb). A sharp pore size distribution of mesopores of 2–10 nm (note Fig. 2Sa) suggests that the nanoparticles exhibited highly ordered pore structure. Decreased crystal size induced by carbon-based surfactants has also been reported in surfactant-assisted sol–gel methods [8–10]. For all the synthesized nanoparticles, large pore volume and relatively high porosity (~50%) was obtained compared to a dense and aggregated reference with porosity of around 25%. Fig. 2Sb clearly shows 4–6 nm pores and randomly oriented 8–10 nm nanocrystallites (see insert at higher magnification).

The degree of agglomeration (DA) of the obtained nanoparticles was calculated by D_{BET}/D_{XRD}. The nonmetal-doped TiO_2 particles show lower degree of agglomeration, according to DA value and ESEM observation for Particle 1 (note Fig. 4S). The large discrepancy between the crystallite size obtained by XRD and BET analysis of the reference TiO_2 sample suggests that it is highly aggregated and is reflected in the value of DA. As mentioned before, the fluorosurfactant works as pore template preventing rapid growth of crystallites and the aggregation of primary particles creating a porous network of nonmetal-doped TiO_2 material. This also resulted in a drastic increase in the specific surface area. The morphology of Particle 1 exhibited a less condensed phase, distinct pore structure and small particle size nanoparticles (note Fig. 3Sa). The lattice fringes can be clearly distinguished providing evidence of high crystallinity, which is in good agreement with the XRD data. The reference TiO_2 sample showed a more condensed phase, less ordered, less defined and a larger particle size (note Fig. 3Sb).

3.3. UV–vis spectra

The UV–vis absorption spectra of Particles 1, 4, 5 and the reference particle prepared by the sol–gel method are shown in Fig. 1. The reference TiO_2 sample showed no absorption towards visible light. Doping of TiO_2 with fluorine did not have any significant effect in the optical absorption capacity towards the visible region. This is in agreement with other results related to fluorine-doped TiO_2 where fluorine does not cause a shift in the absorption edge of TiO_2 [25–28]. When doping with nitrogen, the absorption spectrum is extended to the visible range of 400–500 nm. For N-F-TiO_2, the absorbance is slightly stronger than with nitrogen doping alone. The energy band gap was estimated by plotting $(Ah\nu)^{1/2}$ dependence on photon energy ($h\nu$), assuming indirect band gap [15,24]. The value of the indirect band gap for each nanoparticle was determined by the linear extrapolation in the high slope of the corresponding curve and is provided in the inset in Fig. 1. It shows a clear reduction in the band gap energy for particles doped with nitrogen (2.80 eV) and codoped with fluorine and nitrogen (2.75 eV) compared to the reference with a typical band gap value for TiO_2 (3.00 eV) and fluorine doped (2.99 eV). This denotes the localized nature of nitrogen and fluorine species in the TiO_2 lattice. Nitrogen substitutes some oxygen atoms in the lattice generating localized states up to 0.73 eV on the top of the valence band [11]. Even though fluorine does not improve the absorption of TiO_2 towards visible light; it contributes to the creation of surface oxygen vacancies based on photoluminescence analysis [21,25]. The combination of nitrogen impurity and oxygen vacancies can induce the appearance of an absorption band in the visible region [25,26].

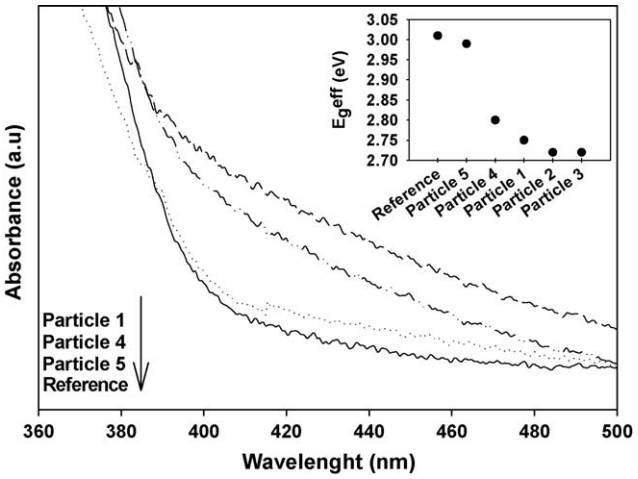

Fig. 1. UV–vis absorption spectra of reference, synthesized TiO_2 with nitrogen, fluorine and nitrogen-fluorine codoped TiO_2.

3.4. XPS analysis

In order to determine the incorporation of nitrogen and fluorine into TiO_2 after heat treatment, the chemical composition was analyzed by XPS. The survey spectra of the Particle 1 (see Fig. 2) contains predominantly Ti, O, N and F elements and a low amount of carbon with a peak at 284.6 eV for C_{1s} core level. In a carbon-doped TiO_2 complex, XPS spectra shows typically three peaks at 284.4 eV, 286.5 eV and 288.4 eV [19]. The first peak is assigned to surface adventitious carbon in undoped TiO_2 which is in agreement with the peak shown in the survey spectra of Particle 1. High-resolution XPS spectra of N_{1s} and F_{1s} are shown in Fig. 2a and b, respectively. Different peaks in the range of 396–404 eV have been observed in different studies and assigned as substitutional and interstitial states of nitrogen in TiO_2 lattice [11]. Both states induce formation of localized states in the gap achieving visible light activity of nitrogen-doped TiO_2. In this study, the core level of N_{1s} shows a wide peak centered at 399.5 eV. A similar binding energy of 399.4 eV for N-doped TiO_2 was reported when employing ethylenediamine compared to 398.6 eV when adding ethanolamine [2]. Choi et al. revealed a binding energy region at 398.3 eV and attributed it to O–Ti–N linkage in the TiO_2 lattice [4]. Therefore, the role of nitrogen needs to be understood in each case since preparation procedures lead to different observations in XPS data. As a result, our observation of N_{1s} at 399.5 eV after high thermal treatment is attributed mainly to nitrogen in the TiO_2 lattice as O–Ti–N which is in agreement with previous studies [4,11,17]. In the core level of F_{1s} in the nonmetal-doped TiO_2 powder, a well-defined peak located at 688.5 eV is attributed to substitutional F atoms in TiO_2 crystal lattice. Other studies [25] reported a peak at 687.8 eV with binding energy calibration with C_{1s} at 284.8 eV, compared to the 284.6 eV performed with this analysis. Fluorine substitution reduces the recombination rate of the electron hole pair due to charge compensation between F^- and Ti^{4+} [21,25]. This can create oxygen vacancies that can act as active sites to produce oxidizing species enhancing photocatalytic activity [25].

For Particle 1, the total atomic concentration of nitrogen was 1.5% and that of fluorine was 4.9%. Nitrogen content of 1.3% and

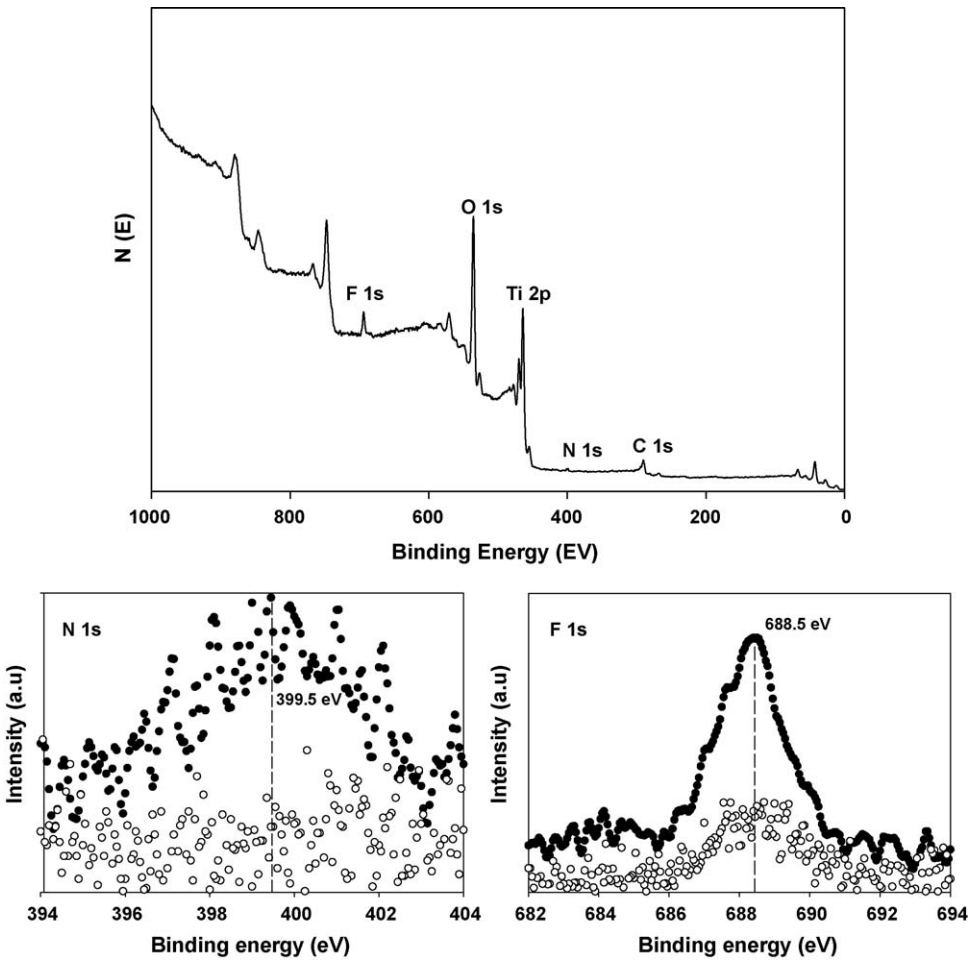

Fig. 2. XPS spectra survey of Particle 1 prepared by the sol–gel method and high resolution XPS of (a) N_{1s} and (b) F_{1s} core levels of Particle 1 and reference TiO_2.

negligible fluorine (0.7%) was detected for Particle 4. Particle 5 showed 3.9% of fluorine and negligible content of nitrogen (0.4%). This is consistent with the atomic concentrations obtained for reference TiO_2, 0.4% of nitrogen and 0.7% of fluorine, probably originated from impurities of the ingredients employed and/or contaminants from air during analysis. A scanning at different angles (15°, 45° and 75°) corresponding to different depth profiles (2–3 nm, 4–5 nm and 6–7 nm) was performed and demonstrated that N and F atoms were incorporated into the lattice of N-F-TiO_2 and distributed throughout the surface depth of the grain. The content was relatively similar at each angle: 1.4 ± 0.22, 1.5 ± 0.23 and 1.4 ± 0.28% for nitrogen and 3.7 ± 0.15, 3.9 ± 0.18 and 3.4 ± 0.21% for fluorine at 15, 45 and 75°, respectively.

3.5. Microcystin-LR degradation under visible irradiation

The results obtained for MC-LR degradation against irradiation time are shown in Fig. 5S. High overall MC-LR degradation can be observed under visible light irradiation with most of the synthesized TiO_2 nanoparticles at pH 3.0 ± 0.1. MC-LR was effectively destroyed with Particle 2 after 300 min of irradiation time. Reference TiO_2 showed no photocatalytic activity under these conditions. Kronos particles vlp 7000 was also tested to determine its photocatalytic efficiency for the destruction of MC-LR and it showed comparable activity to nonmetal-doped TiO_2 nanoparticles employed in this study. Fig. 3a shows the degradation rates of MC-LR after 120 min of reaction time. MC-LR itself does not undergo direct photodegradation with visible light ($\lambda > 420$ nm), as observed in other studies [4]. With TiO_2 nanoparticles doped with either fluorine or nitrogen, a degradation rate of 1.30 ± 0.34 and $1.73 \pm 0.32 \times 10^{-3}$ μM min^{-1} was observed, respectively. This represents a toxin degradation percentage of 11% and 19%, respectively, in the same reaction time. Even though no significant absorbance in the visible light was observed for Particle 4, fluorine-doped TiO_2 might lead to visible photocatalytic activity by the formation of surface oxygen vacancies during surface photochemical process. Surface oxygen vacancies strongly modify the surface band structures with the appearance of intragap states and can lead to the formation of radical species by adsorbing molecular oxygen on the site [24,26]. For Particle 5, the role of nitrogen for band gap narrowing is evident and proven effective for the visible light photocatalytic activation of TiO_2. These results are in agreement with results obtained using N-TiO_2 nanoparticles synthesized at 400 °C by Choi et al. for the destruction of MC-LR at 120 min [4]. When both N and F atoms are present in the TiO_2 lattice, an increase in the MC-LR degradation rate is observed. The toxin degradation percentage for Particles 1, 2 and 3 were 47%, 57% and 29%, respectively, at 120 min of reaction time. The synergistic effect produced by both dopants is clearly exhibited. As the solvent/EDA molar ratio increases, the degradation efficiency and rate increases due to the enhancement of active surface area and pore volume. However, if Particles 3 and 4 with similar surface area are compared (see Table 1), the incorporation of fluorine improved the photocatalytic activity for the degradation of MC-LR. This reveals the synergistic effect of nitrogen and fluorine doping and excludes the possibility of higher degradation rates due only to enhanced structural properties of the synthesized nanomaterial compared to

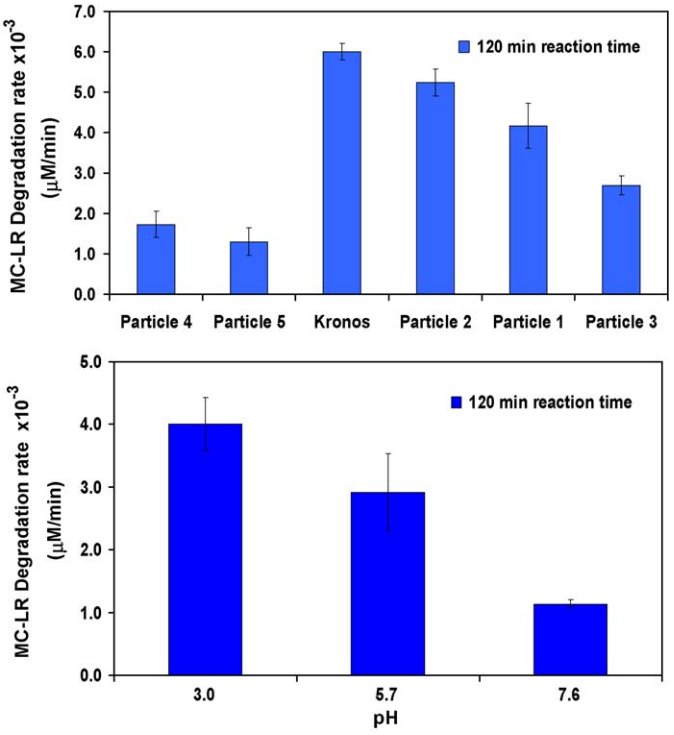

Fig. 3. (a) Performance of different synthesized and commercial TiO_2 at pH 3.0 under visible light irradiation ($\lambda > 420$ nm) for the destruction of MC-LR and (b) MC-LR degradation rate after 120 min of reaction time with nonmetal-doped TiO_2 (Particle 1) at different pH conditions.

reference TiO_2. The surface area of Kronos vlp 7000 was determined to be around 290 m^2/g and a toxin degradation percentage of 70% after 120 min of reaction time was obtained with this catalyst. If MC-LR degradation rate is calculated per unit of surface area, then most of the nonmetal-doped TiO_2 exhibited a higher degradation rate ($5.88 \pm 0.55 \times 10^{-3}$, $6.85 \pm 0.33 \times 10^{-3}$ and $4.51 \pm 0.22 \times 10^{-3}$ $\mu M\ min^{-1}\ m^{-2}$ for Particles 1, 2 and 3, respectively) at 120 min of reaction time compared to Kronos ($4.13 \pm 0.20 \times 10^{-3}$ $\mu M\ min^{-1}\ m^{-2}$) suggesting the benefits of codoping with nitrogen and fluorine and the effectiveness of the sol–gel synthesis route employed.

Electrostatic interactions between the substrate and the catalyst influence the photocatalytic efficiency of the system since oxidizing species are formed mainly at the surface of the catalyst [38]. For pH values between 3 and 12, the ionization of the carboxylic groups, among other functional groups, in the MC-LR structure leads to an overall negatively charge molecule [7]. In contrast, at acidic conditions (pH 3.0) TiO_2 nanoparticles are positively charge according to the point of zero charge (PZC, see Table 1). Faster MC-LR degradation rates were observed under these conditions as a result of the surface attractive forces between MC-LR and the catalyst. At pH 5.7, TiO_2 is relatively in a neutral state compared to the negatively charged MC-LR decreasing the attraction forces between them. This is depicted by the decreased in the degradation rate when the solution pH was increased from 3.0 to 5.7 (see Fig. 3b) employing Particle 1. When the pH is further increased to more basic conditions (pH 7.6), the effect increases since the surface of TiO_2 becomes negatively charged and repulsion forces prevent a strong interaction between the toxin and the catalyst leading to a lower photocatalytic activity, thus, a lower degradation rate of MC-LR.

4. Conclusions

N-F-TiO_2 nanoparticles were successfully synthesized from a modified sol–gel method employing a novel fluorosurfactant as pore template and fluorine dopant and ethylenediamine as nitrogen sources. The nanoparticles exhibited enhanced structural properties such as high surface area, active anatase phase, small crystal size and pore volume and low degree of agglomeration, as well as photocatalytic properties under visible light irradiation compared to the reference TiO_2. The synergistic effect induced by the codoping of TiO_2 with nitrogen and fluorine had significant photocatalytic improvement for the degradation of MC-LR compared to nitrogen or fluorine doping alone. The highest degradation rate was achieved under acidic conditions (pH 3.0 ± 0.1) with nanoparticles containing both F and N atoms. At higher pH values, MC-LR degradation rate decreased indicating pH dependence. These materials can be engineered into flow-through reactors representing a feasible option for solar-driven water treatment technologies or for the remediation of contaminated water with cyanobacterial toxins or other emerging contaminants of concern using visible light-activated TiO_2 photocatalyst under solar irradiation.

Acknowledgments

This work was funded in part by the U.S. Environmental Protection Agency (RD-83322301) and in part by the National Science Foundation through a CAREER award (BES-0448117) to Dionysios D. Dionysiou.

Appendix A. Supplementary data

Supplementary data associated with this article can be found, in the online version, at doi:10.1016/j.cattod.2008.12.022.

References

[1] N. Savage, M.S. Diallo, J. Nanopart. Res. 7 (2005) 331–342.
[2] Y. Liu, J. Li, X. Qiu, C. Burda, J. Photochem. Photobiol., A 190 (2007) 94–100.
[3] E.R. Bandala, M.A. Pelaez, D.D. Dionysiou, S. Gelover, J. Garcia, D. Macias, J. Photochem. Photobiol., A 186 (2007) 357–363.
[4] H. Choi, M.G. Antoniou, M. Pelaez, A.A. De la Cruz, J.A. Shoemaker, D.D. Dionysiou, Environ. Sci. Technol. 41 (2007) 7530–7535.
[5] Q. Yang, H. Choi, D.D. Dionysiou, Appl. Catal., B 74 (2007) 170–178.
[6] H. Choi, E. Stathatos, D.D. Dionysiou, Desalination 202 (2007) 199–206.
[7] M.G. Antoniou, J.A. Shoemaker, A.A. de la Cruz, D.D. Dionysiou, Toxicon 51 (2008) 1103–1118.
[8] Y. Chen, E. Stathatos, D.D. Dionysiou, Surf. Coat. Technol. 202 (2008) 1944–1950.
[9] H. Choi, E. Stathatos, D.D. Dionysiou, Thin Solids Films 510 (2006) 107–114.
[10] H. Choi, E. Stathatos, D.D. Dionysiou, Appl. Catal., B 63 (2006) 60–67.
[11] C. Di Valentin, E. Finazzi, G. Pacchioni, A. Selloni, S. Livraghi, M.C. Paganini, E. Giamello, Chem. Phys. 339 (2007) 44–56.
[12] C. Belver, R. Bellod, A. Fuerte, M. Fernandez-Garcia, Appl. Catal., B 65 (2006) 301–308.
[13] J.L. Gole, J.D. Stout, C. Burda, Y. Lou, X. Che, J. Phys. Chem. B 108 (2004) 1230–1240.
[14] W. Choi, A. Termin, M.R. Hoffmann, J. Phys. Chem. B 98 (1994) 13669–13679.
[15] A.E.J. Gonzalez, S.G. Santiago, Semicond. Sci. Technol. 22 (2007) 709–716.
[16] Y.Q. Wang, X.J. Yu, D.Z. Sun, J. Hazard. Mater. 144 (2007) 328–333.
[17] M. Sathish, B. Viswanathan, R.P. Viswanath, C.S. Gopinath, Chem. Mater. 17 (2005) 6349–6353.
[18] S. Yin, K. Ihara, M. Komatsu, Q. Zhang, F. Saito, T. Kyotani, T. Sato, Solid State Commun. 137 (2006) 132–137.
[19] D. Chen, Z. Jiang, J. Gen, Q. Wang, D. Yang, Ind. Eng. Chem. Res. 47 (2007) 2741–2746.
[20] R. Bacsa, J. Kiwi, T. Ohno, P. Albers, V. Nadtochenko, J. Phys. Chem. B 109 (2005) 5994–6003.
[21] D. Li, H. Haneda, N.K. Labhsetwar, S. Hishita, N. Ohashi, Chem. Phys. Lett. 401 (2005) 579–584.
[22] R. Asahi, T. Morikawa, K. Aoki, Y. Taga, Science 293 (2001) 269–271.
[23] H. Irie, Y. Watanabe, K. Hashimoto, J. Phys. Chem. B 107 (2003) 5483–5486.
[24] A.I. Kontos, A.G. Kontos, Y.S. Raptis, P. Falaras, Phys. Stat. Sol. (RRL) 2 (2008) 83–85.
[25] D. Li, N. Ohashi, S. Hishita, T. Kolodiazhnyi, H. Haneda, J. Solid State Chem. 178 (2005) 3293–3302.
[26] D. Huang, S. Liao, J. Liu, Z. Dang, L. Petrik, J. Photochem. Photobiol., A 184 (2006) 282–288.
[27] Y. Xie, Y. Li, X. Zhao, J. Mol. Catal. A: Chem. 277 (2007) 119–126.
[28] E. Kissa, Fluorinated Surfactants and Repellents, Marcel Dekker, New York, 2001, p. 233.

[29] B. Tan, H.J. Lehmier, S.M. Vyas, B.L. Knutson, S.E. Rankin, Chem. Mater. 17 (2005) 916–925.
[30] B. Tan, A. Dozier, H.J. Lehmier, B.L. Knutson, S.E. Rankin, Langmuir 20 (2004) 6981–6984.
[31] J.L. Blin, M.J. Stebe, Langmuir 108 (2004) 11399–11405.
[32] J.L. Blin, P. Lesieur, M.J. Stebe, Langmuir 20 (2004) 491–498.
[33] M.G. Antoniou, A.A. de la Cruz, D.D. Dionysiou, J. Environ. Eng. 51 (2005) 1239–11243.
[34] P.K.J. Robertson, L.A. Lawton, B. Münch, J. Rouzade, Chem. Commun. 4 (1997) 393–394.
[35] J. Feitz, T.D. Waite, G.J. Jones, B.H. Boyden, P.T. Orr, Environ. Sci. Technol. 33 (1999) 243–249.
[36] U. Schubert, J. Mater. Chem. 15 (2005) 3701–3715.
[37] R. Xie, J.K. Shang, J. Mater. Sci. 45 (2007) 6583–6589.
[38] M.R. Hoffmann, S.T. Martin, W. Choi, D.W. Bahnemann, Chem. Rev. 95 (1995) 69–96.